


## Article

# In Situ Grown 1D/2D Structure of $\text{Dy}_3\text{Si}_2\text{C}_2$ on $\text{SiC}_w$ for Enhanced Electromagnetic Wave Absorption

Gang Qin <sup>1,2</sup>, Yang Li <sup>3</sup>, Wei Zhou <sup>4</sup> , Huidong Xu <sup>2</sup>, Fang Hu <sup>1,\*</sup> and Xiaobing Zhou <sup>1,2,\*</sup>

<sup>1</sup> School of Materials Science and Chemical Engineering, Ningbo University, Ningbo 315211, China; qingang@nimte.ac.cn

<sup>2</sup> Engineering Laboratory of Advanced Energy Materials, Ningbo Institute of Materials Technology and Engineering, Chinese Academy of Sciences, Ningbo 315201, China; xuhuidong@nimte.ac.cn

<sup>3</sup> National Key Laboratory of Science and Technology on High-Strength Structural Materials, Central South University, Changsha 410083, China; liyang16@csu.edu.cn

<sup>4</sup> Hunan Key Laboratory of Applied Environmental Photocatalysis, Changsha University, Changsha 410022, China; zhouwei\_csu@163.com

\* Correspondence: hufang@nbu.edu.cn (F.H.); zhoubx@nimte.ac.cn (X.Z.)

**Abstract:** To improve electromagnetic wave (EMW) absorption performance, a novel nano-laminated  $\text{Dy}_3\text{Si}_2\text{C}_2$  coating was successfully in situ coated on the surface of SiC whisker ( $\text{SiC}_w/\text{Dy}_3\text{Si}_2\text{C}_2$ ) using a molten salt approach. A labyrinthine three-dimensional (3D) net was constructed by the one-dimensional (1D)  $\text{SiC}_w$  coated with the two-dimensional (2D)  $\text{Dy}_3\text{Si}_2\text{C}_2$  layer with a thickness of  $\sim 100$  nm, which significantly improved the EMW absorption properties of  $\text{SiC}_w$ . Compared to pure  $\text{SiC}_w$  with the minimum reflection loss ( $\text{RL}_{\min}$ ) value of  $-10.64$  dB and the effective absorption bandwidth (EAB) of 1.04 GHz for the sample with a thickness of 4.5 mm,  $\text{SiC}_w/\text{Dy}_3\text{Si}_2\text{C}_2$  showed a significantly better EMW absorption performance with  $\text{RL}_{\min}$  of  $-32.09$  dB and wider EAB of 3.76 GHz for thinner samples with a thickness of 1.76 mm. The enhancement of the EMW absorption performance could be ascribed to the improvement of impedance matching, enhanced conductance loss, interfacial polarization as well as multiple scattering. The  $\text{SiC}_w/\text{Dy}_3\text{Si}_2\text{C}_2$  can be a candidate for EMW absorber applications due to its excellent EMW absorption performance and wide EAB for relatively thin samples, light weight, as well as potential oxidation and corrosion resistance at high temperatures.

**Keywords:** SiC whisker;  $\text{Dy}_3\text{Si}_2\text{C}_2$ ; electromagnetic wave absorption; molten salt method



**Citation:** Qin, G.; Li, Y.; Zhou, W.; Xu, H.; Hu, F.; Zhou, X. In Situ Grown 1D/2D Structure of  $\text{Dy}_3\text{Si}_2\text{C}_2$  on  $\text{SiC}_w$  for Enhanced Electromagnetic Wave Absorption. *Materials* **2023**, *16*, 3455. <https://doi.org/10.3390/ma16093455>

Academic Editor: Fernando Julian

Received: 20 March 2023

Revised: 21 April 2023

Accepted: 24 April 2023

Published: 28 April 2023



**Copyright:** © 2023 by the authors. Licensee MDPI, Basel, Switzerland. This article is an open access article distributed under the terms and conditions of the Creative Commons Attribution (CC BY) license (<https://creativecommons.org/licenses/by/4.0/>).

## 1. Introduction

Electromagnetic wave (EMW) radiation pollution seriously endangers human health, as a consequence of the widespread applications of the high frequency electronic devices [1–5]. In recent years, numerous EMW absorption materials have been developed to solve these problems [6,7], including carbon-based materials [8,9], magnetic metal materials [10–12], ferrite and its composites [13–15], and polymer matrix composites [16–18]. However, the poor oxidation resistance of carbon-based materials and polymer matrix composites at high temperatures has impeded their applications, despite their excellent EMW absorption properties [19]. Magnetic materials also cannot be used at high temperatures due to the demagnetization [20]. Furthermore, a relatively high density of ferrite materials also hinders their applications in some special fields, such as aerospace. Therefore, the development of high performance EMW absorption materials with high absorption capability, broad effective absorption bandwidth (EAB), low density as well as small thickness, and excellent oxidation resistance at high temperatures is a critical challenge in this field to minimize EMW radiation pollution.

SiC has been considered a promising candidate for EMW absorbers because it has excellent dielectric properties, high temperature stability, as well as outstanding oxidation and corrosion resistance [21,22]. Most of the works on SiC-based EMW absorption materials

have been focused on the SiC nanoparticles (SiCNP), SiC fibers (SiC<sub>f</sub>), SiC nanowires (SiCNWs), and SiC whiskers (SiC<sub>w</sub>) [23–28]. Among all of them, one-dimensional (1D) SiC<sub>w</sub> or SiCNWs have drawn the most significant attention, since they have large aspect ratio, which is good for dissipating current by providing long transport paths, resulting in a strong conduction loss [29]. Furthermore, a three-dimensional (3D) network can be easily constructed, which is beneficial to improving the EMW absorption performance [27,30]. However, the EMW absorption properties of pure SiC<sub>w</sub> cannot meet the strict requirements of a strong absorption and a broad EAB because of the poor impedance matching and single EMW loss mechanism [31–33]. Therefore, many research works have been conducted to improve the EMW absorption properties of SiC<sub>w</sub>, including elemental doping, surface modification, and fabrication of SiC<sub>w</sub>-based composites [34,35]. For example, Kuang et al. reported that the electrical conductivity of SiC<sub>w</sub> was significantly enhanced by Al-doping. The lowest reflection loss (RL) value was −25.4 dB, and the EAB was 2 GHz when the Al/Si ratio was 0.03/0.97 [29]. In particular, surface modification of SiC<sub>w</sub> has been demonstrated to be an efficient and feasible method for improving the EMW absorption [27,31,36].

Rare earth silicide carbides (RE<sub>3</sub>Si<sub>2</sub>C<sub>2</sub>, where RE is a rare earth element) are a new group of ternary layered structure materials, which are similar to MAX phases (where M is an early transition metal, A is an A-group element, and X is either C or N) [37,38]. RE<sub>3</sub>Si<sub>2</sub>C<sub>2</sub> has been successfully used as the joining layer material and/or sintering additive for SiC-based ceramics and composites due to its ability to form a liquid phase by the eutectic reaction with SiC [39–46]. Furthermore, the addition of a second phase can significantly promote the EMW absorption properties of the resulting composites [47,48]. Our previous work indicated that the EMW absorption properties of SiC<sub>f</sub> can be significantly improved by the incorporation of Y<sub>3</sub>Si<sub>2</sub>C<sub>2</sub> coating on the SiC<sub>f</sub> surface [3]. The minimum RL of SiC<sub>f</sub>/Y<sub>3</sub>Si<sub>2</sub>C<sub>2</sub> was −16.98 dB at a thin thickness of 2.19 mm. Furthermore, compared to the EAB of 1.92 GHz at the thickness of 3.38 mm for pure SiC fiber, SiC<sub>f</sub>/Y<sub>3</sub>Si<sub>2</sub>C<sub>2</sub> shows significantly wider optimal EAB of 5.44 GHz at a much thinner thickness of 2.64 mm [3]. SiC<sub>w</sub> whiskers have a larger aspect ratio compared to the chopped SiC fibers. It is relatively easy to form a 3D net, which is beneficial for increasing the heterogeneous interfaces and multiple reflections and scattering. Therefore, it is expected that SiC<sub>w</sub>/Dy<sub>3</sub>Si<sub>2</sub>C<sub>2</sub> could show even better EMW absorption properties when compared to SiC<sub>f</sub>/Y<sub>3</sub>Si<sub>2</sub>C<sub>2</sub>.

In this work, the two-dimensional (2D) Dy<sub>3</sub>Si<sub>2</sub>C<sub>2</sub> coating is formed on the one-dimensional (1D) SiC<sub>w</sub> surface by the molten salt method to improve the EMW absorption properties. Combining Dy<sub>3</sub>Si<sub>2</sub>C<sub>2</sub> with SiC<sub>w</sub> not only effectively improved the impedance matching but also provided a large number of heterogeneous interfaces as well as enhanced interface polarization loss. At the same time, the stacking effect of one-dimensional structures builds an efficient three-dimensional conductive network that enhances resistance loss. Furthermore, the two-dimensional layered structure of Dy<sub>3</sub>Si<sub>2</sub>C<sub>2</sub> can improve multiple reflections, which is beneficial to improving the EMW absorption properties. Microstructure, phase composition, dielectric, and EMW absorption properties of the as-obtained SiC<sub>w</sub>/Dy<sub>3</sub>Si<sub>2</sub>C<sub>2</sub> coated whiskers were investigated. The possible EMW absorption mechanism of SiC<sub>w</sub>/Dy<sub>3</sub>Si<sub>2</sub>C<sub>2</sub> was summarized. EMW absorption properties of the as-obtained SiC<sub>w</sub>/Dy<sub>3</sub>Si<sub>2</sub>C<sub>2</sub> were compared to the previously reported materials.

## 2. Experimental Procedure

### 2.1. Materials and Experiments

DyH<sub>2</sub> powder with a purity of 99.9% and a mean particle size of ~75 μm was purchased from Institute of Hunan rare earth metal materials Co., Ltd., Changsha, China. SiC whiskers (Union Materials Co., Daegu, Republic of Korea) with a diameter of 0.4–0.9 μm and a length of 6–120 μm; NaCl; and KCl powders (purity: 99.5%, mean particle size: 75 μm; Sinopharm Chemical Reagent Co., Ltd., Shanghai, China) were used as the raw materials.

The DyH<sub>2</sub>, SiC<sub>w</sub>, NaCl, and KCl powders with the molar ratio of DyH<sub>2</sub>: SiC<sub>w</sub> = 1:4 and NaCl:KCl = 1:1 were mixed for 30 min in an Ar atmosphere in a home-made glove box. The mixed DyH<sub>2</sub>, SiC<sub>w</sub>, NaCl, and KCl powders were heated to a target temperature of 1000 °C

in the molten salt furnace. The holding time was set 5 h. The heating and cooling rate was 5 °C/min. The as-obtained samples were washed and filtered using deionized water several times. The in situ coated  $\text{SiC}_w/\text{Dy}_3\text{Si}_2\text{C}_2$  powder can be obtained after drying 12 h at 60 °C in a vacuum oven.

## 2.2. Characterizations

The phase compositions of the as-obtained  $\text{SiC}_w/\text{Dy}_3\text{Si}_2\text{C}_2$  were detected using an X-ray diffractometer (XRD: D8 Advance, Bruker AXS, Karlsruhe, Germany) using  $\text{Cu K}\alpha$  radiation ( $\lambda = 1.5406 \text{ \AA}$ ). The operating current and voltage were 40 mA and 40 kV, respectively. The step scan and step time was  $0.02^\circ 2\theta$  and 0.2 s, respectively. The microstructure of the  $\text{SiC}_w/\text{Dy}_3\text{Si}_2\text{C}_2$  powders was observed using a scanning electron microscope (SEM, 8230, Hitachi, Tokyo, Japan). The microstructure and phase compositions of the  $\text{Dy}_3\text{Si}_2\text{C}_2$  coating were further investigated using a transmission electron microscope (TEM, Talos F200X, Thermo Fisher Scientific, Waltham, MA, USA) equipped with an energy dispersive spectroscopy (EDS) system. The samples for TEM observations were prepared using the focused ion beam (FIB, Auriga, Carl Zeiss, Jena, Germany) technique. The complex permittivity and complex permeability were measured at a frequency range from 2 to 18 GHz using a Network Analyzer of Agilent N5230A. In order to measure the complex permittivity and complex permeability,  $\text{SiC}_w/\text{Dy}_3\text{Si}_2\text{C}_2$  powder was mixed with 50 wt.% paraffin with a size of an inner and outer diameter of 3 and 7 mm as well as a thickness of 2 mm, respectively. For the sake of comparison, the electromagnetic properties of the pure SiC whiskers were detected using the same method.

## 3. Results and Discussion

### 3.1. Microstructure and Phase Composition of $\text{SiC}_w/\text{Dy}_3\text{Si}_2\text{C}_2$

Figure 1 presents the XRD patterns of the pure SiC whiskers and the as-obtained  $\text{SiC}_w/\text{Dy}_3\text{Si}_2\text{C}_2$  whiskers.

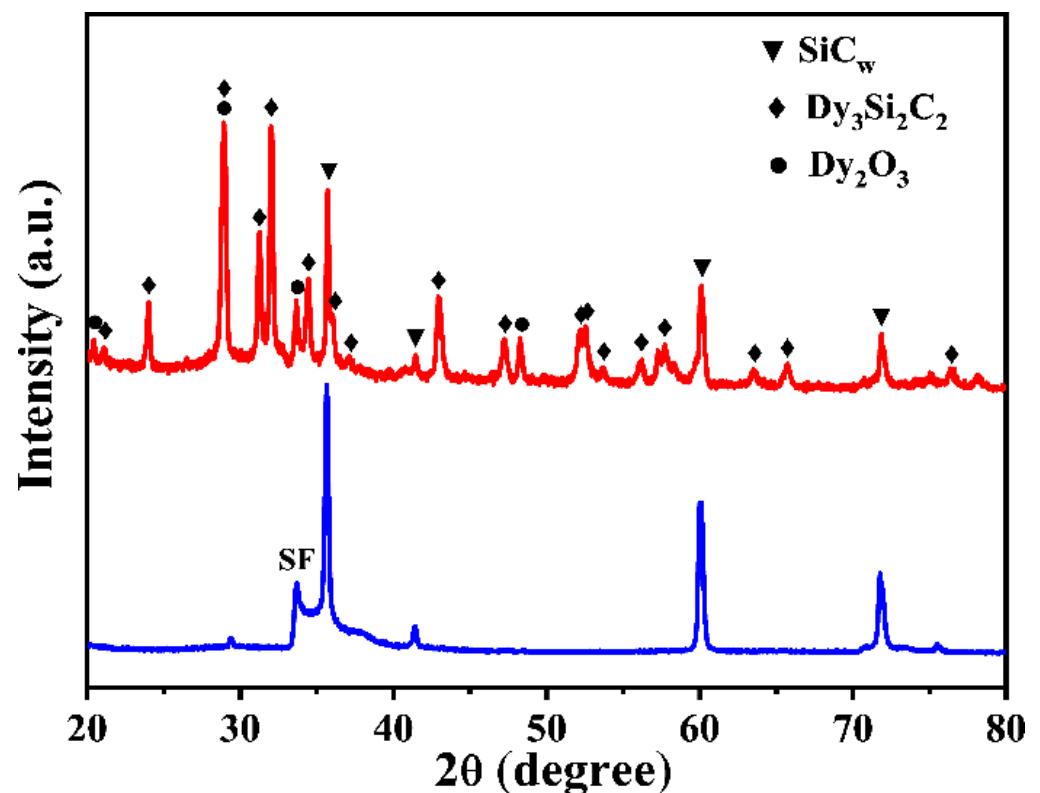
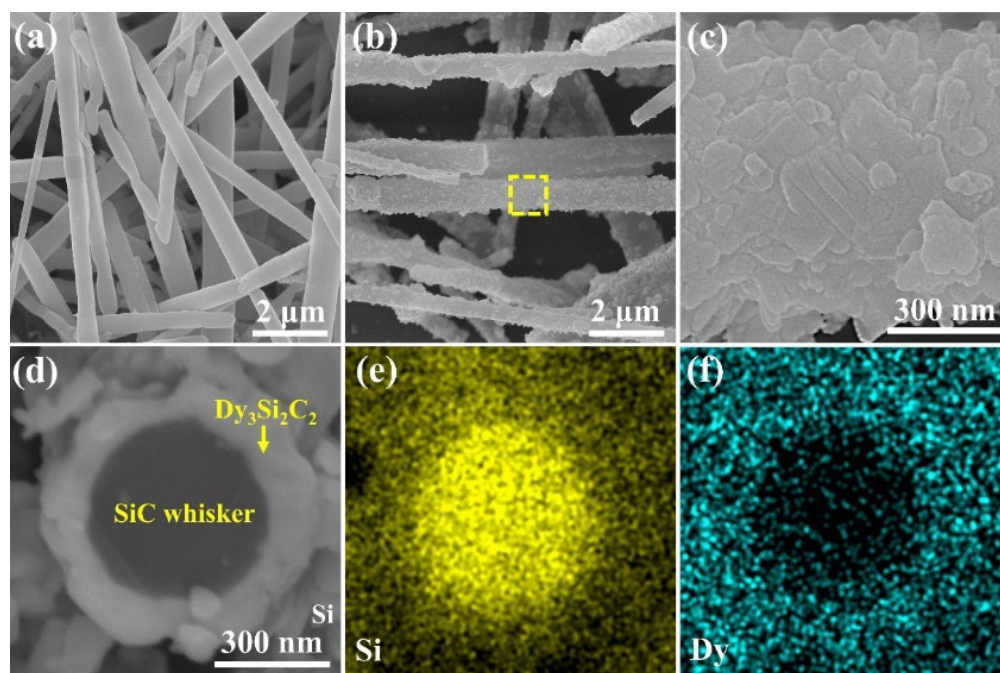


Figure 1. XRD patterns of pure SiC and  $\text{SiC}_w/\text{Dy}_3\text{Si}_2\text{C}_2$  whiskers.

The XRD pattern of pure SiC whiskers indicated that they are formed by the 3C-SiC phase (JCPDS No. 75-0254). A small peak at approximately  $33.5^\circ$  corresponds to the stacking faults, which spontaneously formed during the growing process of SiC whiskers. The XRD pattern of the SiC<sub>w</sub>/Dy<sub>3</sub>Si<sub>2</sub>C<sub>2</sub> powder revealed that besides SiC<sub>w</sub>, it also contained characteristic peaks of Dy<sub>3</sub>Si<sub>2</sub>C<sub>2</sub> (JCPDS No. 97-005-1299) along with some impurities of Dy<sub>2</sub>O<sub>3</sub> (JCPDS No. 97-018-5606). This confirmed that the Dy<sub>3</sub>Si<sub>2</sub>C<sub>2</sub> modification of SiC whiskers was successfully obtained.

Figure 2 shows the SEM images of both SiC<sub>w</sub> and SiC<sub>w</sub>/Dy<sub>3</sub>Si<sub>2</sub>C<sub>2</sub> whiskers.



**Figure 2.** SEM images of pure SiC<sub>w</sub> (a) and SiC<sub>w</sub>/Dy<sub>3</sub>Si<sub>2</sub>C<sub>2</sub> (b,c), (c) is the high magnification SEM image of the yellow dashed area in (b), cross-section back scattered SEM image of SiC<sub>w</sub>/Dy<sub>3</sub>Si<sub>2</sub>C<sub>2</sub> (d) and its corresponding EDS elemental distribution of Si (e) and Dy (f).

The diameter of the pure SiC whiskers was  $\sim 500$  nm. A dense 2D structure Dy<sub>3</sub>Si<sub>2</sub>C<sub>2</sub> coating with a structure of randomly oriented nano-laminated sheets was in situ coated on the surface of SiC whiskers (Figure 2b,c). The thickness of Dy<sub>3</sub>Si<sub>2</sub>C<sub>2</sub> coating was around 100 nm, as shown in the SEM image of the fracture surface of the SiC<sub>w</sub>/Dy<sub>3</sub>Si<sub>2</sub>C<sub>2</sub> whisker (Figure 2d). The corresponding elemental distribution of Si and Dy indicated that most of the Dy<sub>3</sub>Si<sub>2</sub>C<sub>2</sub> was homogeneously coated on the surface of SiC whisker (Figure 2e,f).

To further confirm the microstructure and phase composition of the Dy<sub>3</sub>Si<sub>2</sub>C<sub>2</sub> coating, semi-quantitative EDS and high-resolution transmission electron microscope (HR-TEM) analysis along with selected-area electron diffraction (SAED) were performed. Figure 3 presents a high-angle annular dark-field (HAADF) image of the as-synthesized SiC<sub>w</sub>/Dy<sub>3</sub>Si<sub>2</sub>C<sub>2</sub> and the corresponding Dy, Si, C, and O elemental distributions, respectively.



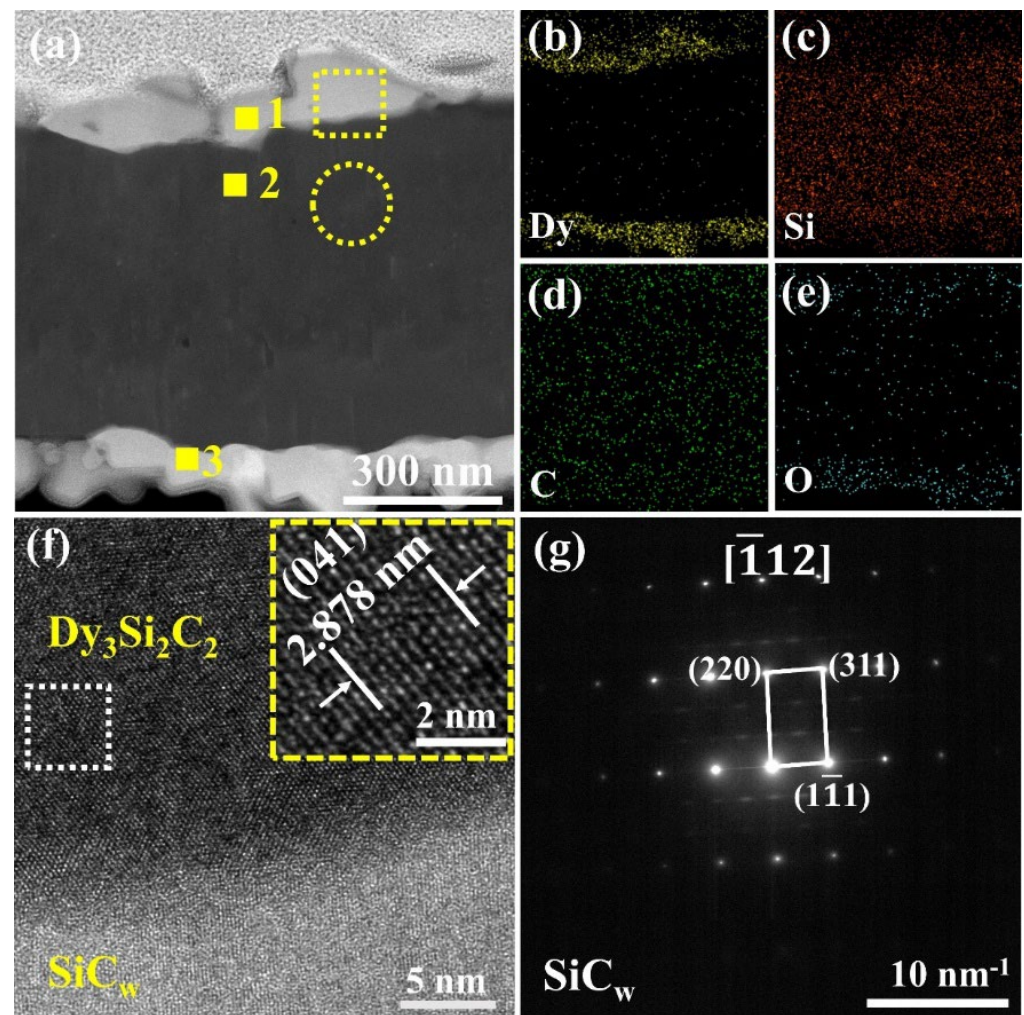


**Figure 3.** (a) HAADF image of the as-synthesized  $\text{SiC}_w/\text{Dy}_3\text{Si}_2\text{C}_2$  and the corresponding EDS mapping of (b) Dy, (c) Si, (d) C, and (e) O, (f) HR-TEM image of the  $\text{Dy}_3\text{Si}_2\text{C}_2$  coating, as highlighted by a yellow rectangle in (a), and (g) the SAED pattern taken from the area highlighted by the yellow circle in (a).

The semiquantitative EDS analysis results of areas 1–3 are shown in Table 1, suggesting the presence of  $\text{SiC}$ ,  $\text{Dy}_3\text{Si}_2\text{C}_2$ , and/or  $\text{Dy}_2\text{O}_3$ .

**Table 1.** EDS results collected from points 1–3 in Figure 3a.

No.	Composition in Atomic %				Probable Phases
	Dy	Si	C	O	
1	45.92	23.11	15.72	15.25	$\text{Dy}_3\text{Si}_2\text{C}_2$ , $\text{Dy}_2\text{O}_3$
2	0.39	59.29	36.12	4.20	$\text{SiC}_w$
3	42.11	22.98	16.99	17.93	$\text{Dy}_3\text{Si}_2\text{C}_2$ , $\text{Dy}_2\text{O}_3$

Furthermore, the HR-TEM image of the interface between  $\text{SiC}_w$  and  $\text{Dy}_3\text{Si}_2\text{C}_2$  coating is shown in Figure 3f. The lattice fringe spacing was 0.2878 nm, which can be assigned to the (041) planes of  $\text{Dy}_3\text{Si}_2\text{C}_2$ . Therefore, taking into account all the results obtained by XRD, EDS, and HR-TEM analysis, it can be concluded that a dense  $\sim 100 \text{ nm}$   $\text{Dy}_3\text{Si}_2\text{C}_2$  coating was successfully fabricated on the surface of  $\text{SiC}_w$  using the molten salt approach.

The formation process of the  $\text{Dy}_3\text{Si}_2\text{C}_2$  coating using the molten salt approach is similar to the formation mechanism of  $\text{Y}_3\text{Si}_2\text{C}_2$  and  $\text{Pr}_3\text{Si}_2\text{C}_2$  powders [45,48]. First,  $\text{DyH}_2$

decomposed to Dy and released  $H_2$  [49]. The Dy element diffused to the surface of SiC whiskers via the liquid molten salt, and then the  $Dy_3Si_2C_2$  coating was formed. The main reactions can be summarized as follow:



On the other hand, the potential formation barrier of the  $Dy_3Si_2C_2$  could decline because the surface energy of both  $DyH_2$  and  $SiC_w$  could be remarkably promoted by polarization effect of the molten salt [50,51]. In addition, the diffusion rate of the Dy, Si, and C atoms can be obviously promoted in the liquid molten salt reaction medium. Therefore, the  $Dy_3Si_2C_2$  coating can be in situ formed on the surface of SiC whiskers at a relatively low temperature (1000 °C) and adhered well to the surface of  $SiC_w$ .

### 3.2. Dielectric Properties of $SiC_w/Dy_3Si_2C_2$

The EMW absorption property of materials is mainly confirmed by their complex permittivity and permeability. Meanwhile, good impedance matching between absorbing materials and free space can make EMW incident into materials with less reflection. While  $SiC_w$  and  $SiC_w/Dy_3Si_2C_2$  are nonmagnetic materials, the real ( $\mu'$ ) and imaginary ( $\mu''$ ) parts of the complex permeability is around 1 and 0, respectively (not shown here). Therefore, the EMW absorption capability of  $SiC_w$  and  $SiC_w/Dy_3Si_2C_2$  is highly dependent on their complex permittivity. The real ( $\epsilon'$ ) and imaginary ( $\epsilon''$ ) parts of complex permittivity of the pure  $SiC_w$  and  $SiC_w/Dy_3Si_2C_2$  whiskers are shown in Figure 4.

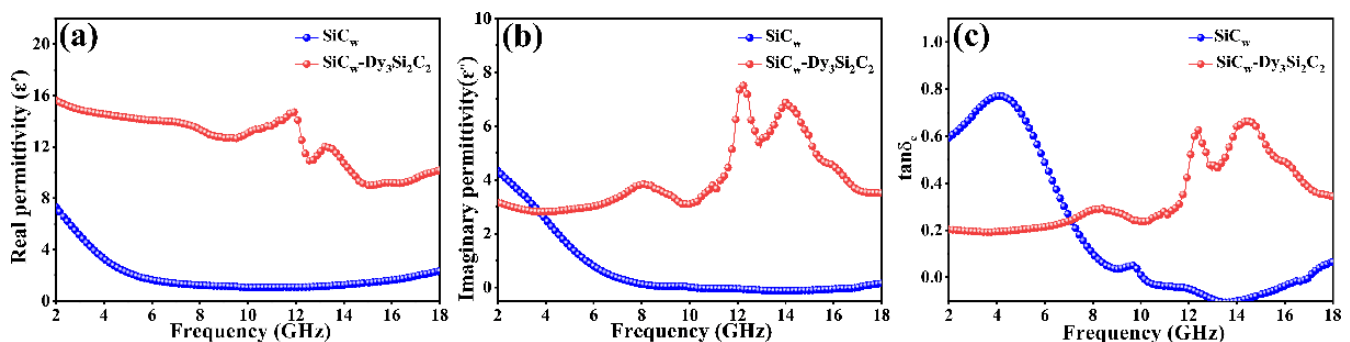


**Figure 4.** Real (a) and imaginary (b) parts of the complex permittivity, as well as the loss angle (c) of the pure  $SiC_w$  and  $SiC_w/Dy_3Si_2C_2$  whiskers.

Most of the real ( $\epsilon'$ ) and imaginary ( $\epsilon''$ ) parts of the complex permittivity of  $SiC_w/Dy_3Si_2C_2$  were higher than that of pure  $SiC_w$ , indicating that the  $Dy_3Si_2C_2$  coating could promote the dielectric properties of  $SiC_w$ .

According to the Debye theory,  $\epsilon'$  and  $\epsilon''$  can be calculated by the following equations [52]:

$$\epsilon' = \epsilon_\infty + (\epsilon_s - \epsilon_\infty) / (1 + (\omega\tau)^2) \quad (3)$$

$$\epsilon'' = (\epsilon_s - \epsilon_\infty) / (1 + (\omega\tau)^2) + \delta_{ac} / \omega\epsilon_0 = \epsilon_p'' + \epsilon_c'' \quad (4)$$

where  $\epsilon_0$ ,  $\epsilon_s$ , and  $\epsilon_\infty$  represent free space dielectric constant, the permittivity in static state, and light frequency, respectively.  $\omega$  and  $\tau$  are angular frequency and polarization relaxation time, respectively.  $\sigma$  is electric conductivity.  $\epsilon_p''$  and  $\epsilon_c''$  correspond to the contributions to  $\epsilon''$  from polarization loss and conductance loss, which are associated with  $\sigma$ . Generally, the real part of the permittivity signifies the storage capability of the dielectric energy, while the imaginary part of the permittivity stands for the loss of dielectric energy [53]. Thus, the improvement of  $\epsilon'$  can be ascribed to the interfacial polarization caused by the

improved heterogeneous interfaces in  $\text{SiC}_w/\text{Dy}_3\text{Si}_2\text{C}_2$  whiskers, which were generated by the incorporation of nano-laminated (2D)  $\text{Dy}_3\text{Si}_2\text{C}_2$  coating on the surface of  $\text{SiC}_w$ . The enhancement of  $\epsilon''$  was mainly decided by the increasing of the electrical conductivity ( $\sigma$ ), where  $\sigma$  can be confirmed by the follow equation [54]:

$$\sigma = 2\pi\epsilon_0\epsilon\epsilon'' \quad (5)$$

where  $\epsilon_0$  represents the permittivity in a vacuum.

The electrical conductivity of  $\text{SiC}_w/\text{Dy}_3\text{Si}_2\text{C}_2$  was higher than that of pure  $\text{SiC}_w$ , as shown in Figure 5a.

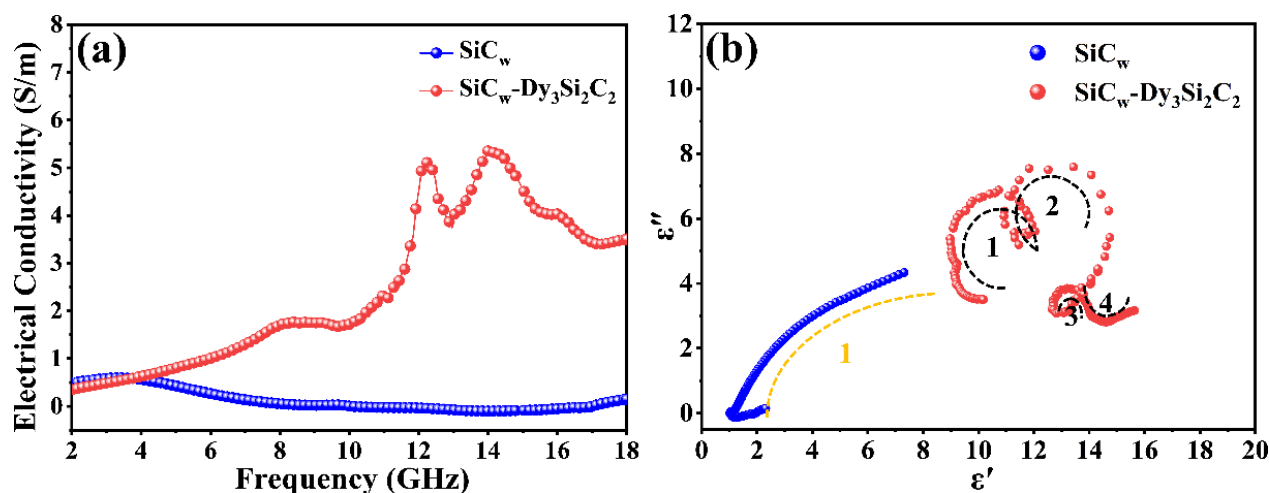


**Figure 5.** Electrical conductivity (a,b) Cole–Cole curves of the pure  $\text{SiC}_w$  and  $\text{SiC}_w/\text{Dy}_3\text{Si}_2\text{C}_2$ .

This can be mainly attributed to the metallic conductivity characteristic of the 2D structural  $\text{Dy}_3\text{Si}_2\text{C}_2$  coating, as the coating formed a net structure, increasing the transmission channels of carriers [55]. In addition, both  $\epsilon'$  and  $\epsilon''$  of  $\text{SiC}_w/\text{Dy}_3\text{Si}_2\text{C}_2$  showed a fluctuation corresponding to the resonance, while this was not observed for the pure  $\text{SiC}_w$ . The permittivity of the  $\text{SiC}_w/\text{Dy}_3\text{Si}_2\text{C}_2$  whiskers showed typical nonlinear resonant characteristics, indicating the existence of polarization and relaxation behavior, which implied better dielectric loss performance in the corresponding frequency range. The Cole–Cole semicircle was used to investigate the relaxation polarization process. According to the Debye theory, the relationship between  $\epsilon'$  and  $\epsilon''$  can be expressed by Equation (6) [56]:

$$(\epsilon'' - (\epsilon_s + \epsilon_\infty)/2)^2 + \epsilon'' = (\epsilon_s - \epsilon_\infty)/2 \quad (6)$$

The Cole–Cole curves of pure  $\text{SiC}_w$  and  $\text{SiC}_w/\text{Dy}_3\text{Si}_2\text{C}_2$  are shown in Figure 5b. Each Deby relaxation process is manifested by one Cole–Cloe semicircle [55,56]. There was only one Cole–Cole semicircle observed in pure  $\text{SiC}_w$ , indicating one relaxation process, while four semicircles were observed in  $\text{SiC}_w/\text{Dy}_3\text{Si}_2\text{C}_2$ , confirming the improvement of dielectric loss capacity in  $\text{SiC}_w/\text{Dy}_3\text{Si}_2\text{C}_2$ . The improvement of the relaxation process of  $\text{SiC}_w/\text{Dy}_3\text{Si}_2\text{C}_2$  was mainly caused by the significantly increased interface relaxation, which resulted from the improved number of heterogeneous interfaces in  $\text{SiC}_w/\text{Dy}_3\text{Si}_2\text{C}_2$ .

### 3.3. Electromagnetic Wave Absorption Performance

Reflection loss (RL) and effective absorption bandwidth (EAB, the corresponding frequency range of  $\text{RL} < -10$  dB, which presents more than 90% EMW energy absorbed) are usually used to evaluate the EMW absorption performance of materials. According to

the transmission line theory, the RL values of SiC<sub>w</sub> and SiC<sub>w</sub>/Dy<sub>3</sub>Si<sub>2</sub>C<sub>2</sub> can be calculated by the following equations [57–59]:

$$RL(dB) = 20 \log |(Z_{in} - Z_0) / (Z_{in} + Z_0)| \quad (7)$$

$$Z_{in} = Z_0 \sqrt{\mu_r / \epsilon_r} \tanh[j(2\pi f d / c) \sqrt{\mu_r \epsilon_r}] \quad (8)$$

$$Z_0 = \sqrt{\mu_r / \epsilon_r} \quad (9)$$

where  $Z_0$  and  $Z_{in}$  is space free impedance and input impedance, respectively.  $c$ ,  $d$ , and  $f$  are speed of light, thickness, and frequency, respectively.  $\mu_r = \mu' - j\mu''$  and  $\epsilon_r = \epsilon' - j\epsilon''$  represent the complex permeability and permittivity of material.

Figure 6 shows the 3D and 2D plots of RL values at the frequency range of 2 to 18 GHz at different thicknesses of the SiC<sub>w</sub> and SiC<sub>w</sub>/Dy<sub>3</sub>Si<sub>2</sub>C<sub>2</sub> samples.

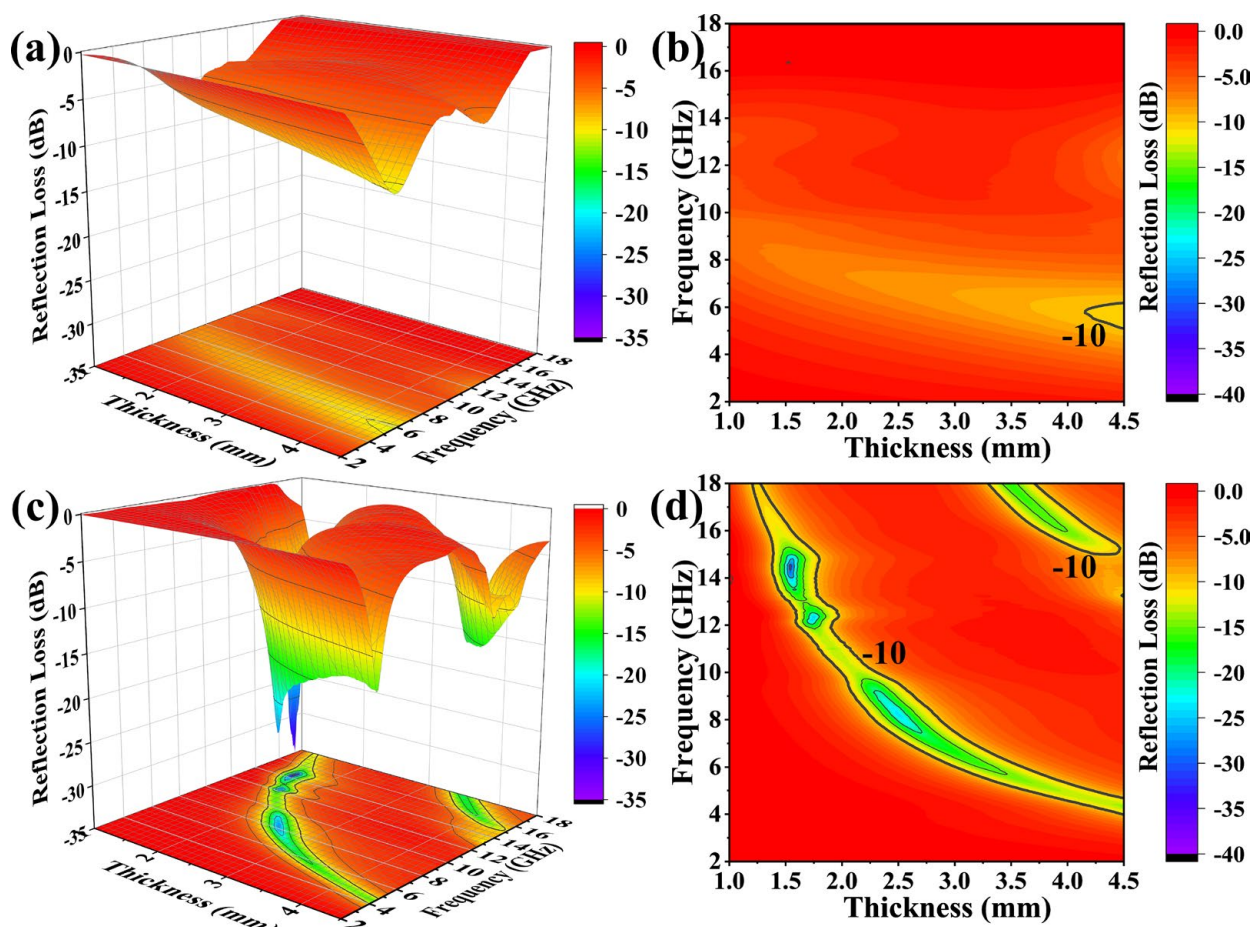


**Figure 6.** 3D and 2D patterns of RL values at the frequency range of 2 to 18 GHz for different thicknesses of SiC<sub>w</sub> (a,b) and SiC<sub>w</sub>–Dy<sub>3</sub>Si<sub>2</sub>C<sub>2</sub> samples (c,d).

The minimum RL ( $RL_{min}$ ) value of the pure SiC<sub>w</sub> is  $-10.64$  dB at the frequency of 5.52 GHz with the 4.5 mm sample thickness. After coating of SiC<sub>w</sub> with 2D Dy<sub>3</sub>Si<sub>2</sub>C<sub>2</sub> sheets, the  $RL_{min}$  value was improved to  $-32.09$  dB at the frequency of 14.48 GHz for the 1.54 mm sample thickness. For convenience of comparison, the selected theoretical calculated RL of pure SiC<sub>w</sub> and SiC<sub>w</sub>/Dy<sub>3</sub>Si<sub>2</sub>C<sub>2</sub> with different thicknesses in the frequency range of 2 to 18 GHz is shown in Figure 7a,b.



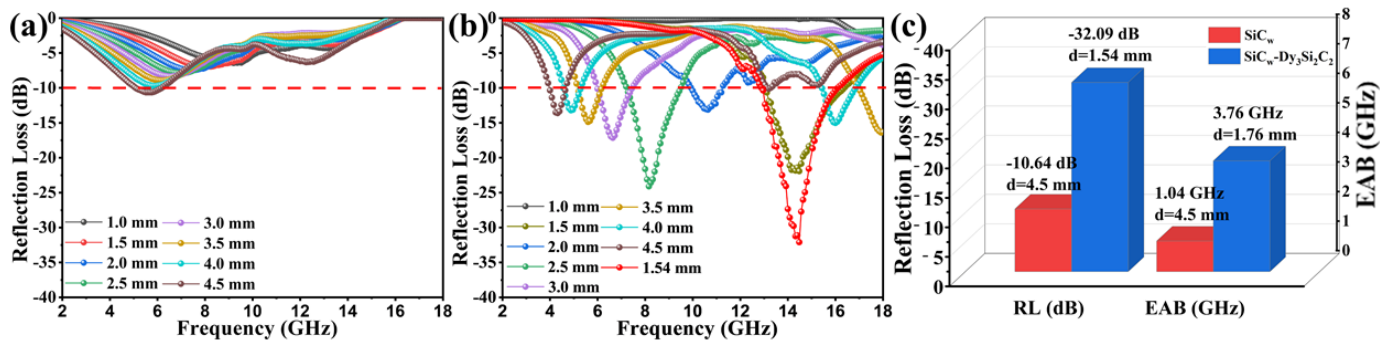


**Figure 7.** RE values at the frequency range of 2 to 18 GHz for different thicknesses of the SiC<sub>w</sub> (a) and SiC<sub>w</sub>/Dy<sub>3</sub>Si<sub>2</sub>C<sub>2</sub> samples (b), (c) comparison of the RL<sub>min</sub> and EAB of the pure SiC<sub>w</sub> and SiC<sub>w</sub>–Dy<sub>3</sub>Si<sub>2</sub>C<sub>2</sub> samples.

It is obvious that the EAB of SiC<sub>w</sub>/Dy<sub>3</sub>Si<sub>2</sub>C<sub>2</sub> is much wider than that of SiC<sub>w</sub> for the samples with the thickness range of 1 to 4.5 mm at the frequency ranging from 2 to 18 GHz. The widest EAB can be as high as 3.76 GHz for thin SiC<sub>w</sub>/Dy<sub>3</sub>Si<sub>2</sub>C<sub>2</sub> samples with the thickness of 1.76 mm (Figure 7c). However, the widest EAB of pure SiC<sub>w</sub> is only 1.04 GHz for the sample with a thickness of 4.5 mm (Figure 7c). This indicates that the Dy<sub>3</sub>Si<sub>2</sub>C<sub>2</sub> coating can significantly improve the EMW absorption properties of SiC<sub>w</sub>.

In order to reveal the intrinsic reason for the improved EMW absorption performance for SiC<sub>w</sub>/Dy<sub>3</sub>Si<sub>2</sub>C<sub>2</sub>, the impedance match ( $Z$ ) as well as the attenuation constant ( $\alpha$ ) were calculated.  $Z$  was confirmed by the following equation [60]:

$$Z = |Z_{in}/Z_0| = \sqrt{\mu_r/\epsilon_r} \tanh[j(2\pi f d/c) \sqrt{\mu_r \epsilon_r}] \quad (10)$$

A favorable impedance match is the basic requirement to obtain an excellent EMW absorption performance, which ensures the EMW can enter materials instead of being reflected [61–64]. According to Equation (10), when the input impedance ( $Z_{in}$ ) is infinitely close to the air impedance ( $Z_0$ ), the ideal impedance matching can be obtained. Figure 8a,b presents the calculated  $Z$  values of the pure SiC<sub>w</sub> and SiC<sub>w</sub>/Dy<sub>3</sub>Si<sub>2</sub>C<sub>2</sub> samples with the thickness of 1–4.5 mm at the frequency ranging from 2 to 18 GHz.

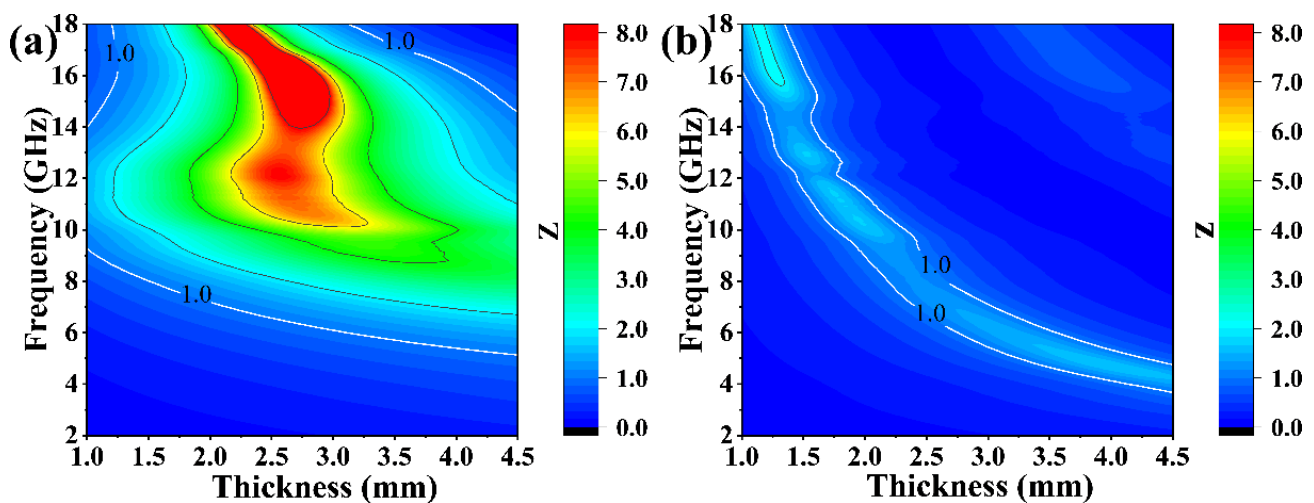


**Figure 8.** 2D patterns of  $Z$  value of SiC<sub>w</sub> (a) and SiC<sub>w</sub>/Dy<sub>3</sub>Si<sub>2</sub>C<sub>2</sub> (b).

The frequency range with good impedance match ( $Z$ -value is close to 1) of SiC<sub>w</sub>/Dy<sub>3</sub>Si<sub>2</sub>C<sub>2</sub> was much larger than that of pure SiC<sub>w</sub>, which indicates that the impedance match of the SiC<sub>w</sub> was well improved by the Dy<sub>3</sub>Si<sub>2</sub>C<sub>2</sub> coating. Therefore, the EMW can enter the

SiC<sub>w</sub>/Dy<sub>3</sub>Si<sub>2</sub>C<sub>2</sub> sample, while most of the EMW was reflected in the case of pure SiC<sub>w</sub> due to the poor impedance matching.

Furthermore, to evaluate the attenuation ability of EMW energy of the samples, the  $\alpha$  (Figure 9) was evaluated by the following formula [53]:

$$\alpha = \frac{\sqrt{2}\pi f}{c} \sqrt{(\mu''\epsilon'' - \mu'\epsilon') + \sqrt{(\mu''\epsilon'' - \mu'\mu')^2 + (\mu'\epsilon'' - \mu''\epsilon')^2}} \quad (11)$$

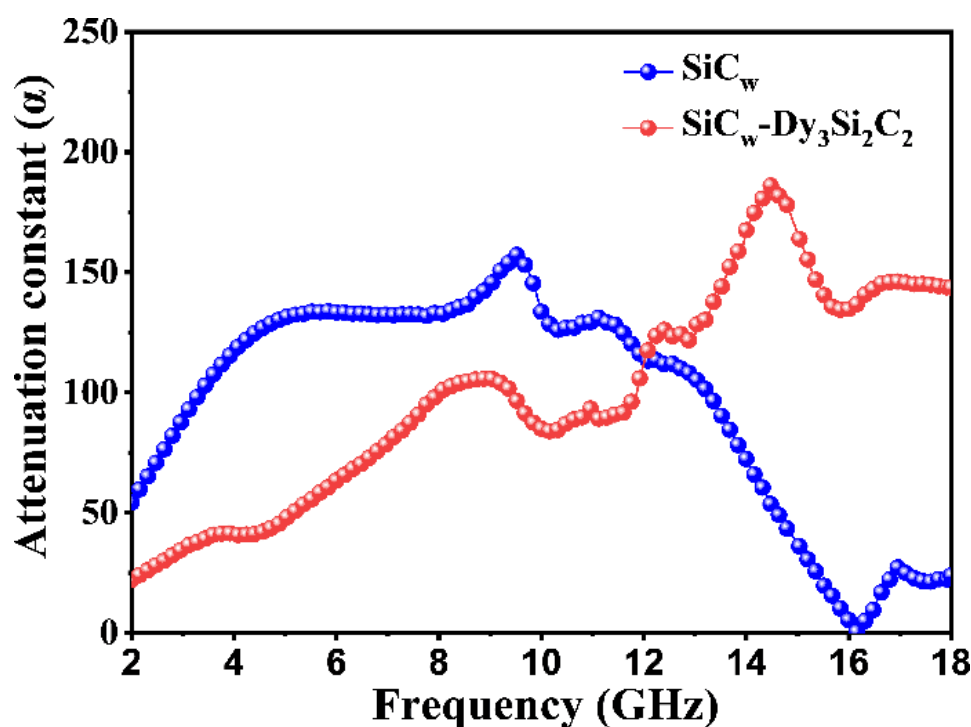


**Figure 9.** Attenuation constant of pure SiC<sub>w</sub> and SiC<sub>w</sub>/Dy<sub>3</sub>Si<sub>2</sub>C<sub>2</sub> at the frequency range from 2 to 18 GHz.

A larger value of  $\alpha$  implies a stronger attenuation ability [65]. The sole high dielectric loss of SiC<sub>w</sub> at a low frequency resulted in a high attenuation constant, which meant that most of the EMW was reflected. This is in good agreement with the poor impedance matching of the SiC<sub>w</sub> sample. On the other hand, the introduction of the nano-laminated (2D) Dy<sub>3</sub>Si<sub>2</sub>C<sub>2</sub> coating significantly improved the impedance match as well as the attenuation ability of the SiC<sub>w</sub>/Dy<sub>3</sub>Si<sub>2</sub>C<sub>2</sub>. As a result, the EMW absorption property was significantly improved.

The possible EMW absorption mechanism of SiC<sub>w</sub>/Dy<sub>3</sub>Si<sub>2</sub>C<sub>2</sub> is illustrated in Figure 10.

Firstly, the favorable impedance matching suggests that the majority of the EMW can enter the SiC<sub>w</sub>/Dy<sub>3</sub>Si<sub>2</sub>C<sub>2</sub> sample, while just a small part of the EMW is reflected. This is the premise of excellent EMW absorption performance of the material. Secondly, the metallic conductivity characteristic of Dy<sub>3</sub>Si<sub>2</sub>C<sub>2</sub> coating improved the electrical conductivity of SiC<sub>w</sub>/Dy<sub>3</sub>Si<sub>2</sub>C<sub>2</sub>, which enhanced the conductance loss by improving the electron transition channel in SiC<sub>w</sub>/Dy<sub>3</sub>Si<sub>2</sub>C<sub>2</sub>. Thirdly, a large number of heterogeneous interfaces in the SiC<sub>w</sub>/Dy<sub>3</sub>Si<sub>2</sub>C<sub>2</sub> sample, such as Dy<sub>3</sub>Si<sub>2</sub>C<sub>2</sub>/Dy<sub>3</sub>Si<sub>2</sub>C<sub>2</sub>, SiC<sub>w</sub>/Dy<sub>3</sub>Si<sub>2</sub>C<sub>2</sub>, and SiC<sub>w</sub>/SiC<sub>w</sub>, significantly increased the interfacial polarization and hopping electrons between Dy<sub>3</sub>Si<sub>2</sub>C<sub>2</sub> nanosheets. This is beneficial for the improvement of the dielectric loss of the material. Finally, the high aspect ratio of SiC<sub>w</sub> with the 2D nano-laminated Dy<sub>3</sub>Si<sub>2</sub>C<sub>2</sub> coating constructed a 3D microstructure and formed an effective conductive network, resulting in the enhancement of multiple scattering and reflections. Therefore, the excellent EMW absorption performance of SiC<sub>w</sub>/Dy<sub>3</sub>Si<sub>2</sub>C<sub>2</sub> was attributed to the synergistic effect of fa-

avorable impedance matching, enhanced conductance loss, interfacial polarization, dipole polarization, and multiple scattering and reflections.

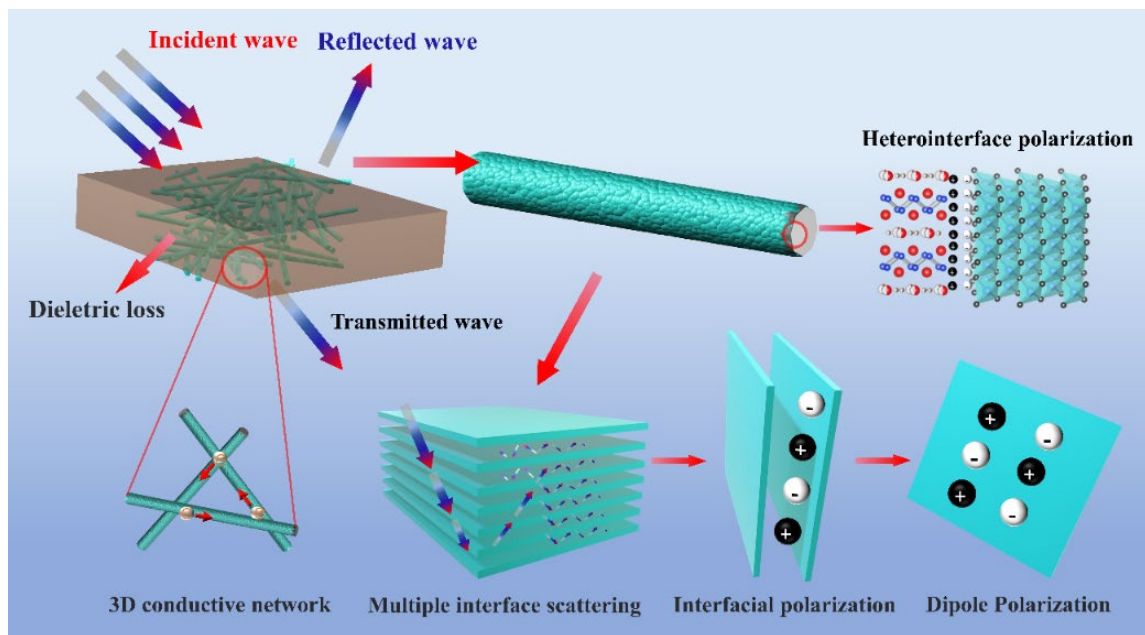


Figure 10. The EMW absorption mechanism of SiC<sub>w</sub>/Dy<sub>3</sub>Si<sub>2</sub>C<sub>2</sub>.

The EMW absorption property of SiC<sub>w</sub>/Dy<sub>3</sub>Si<sub>2</sub>C<sub>2</sub> is better when compared to most of the previously reported materials, as shown in Figure 11.

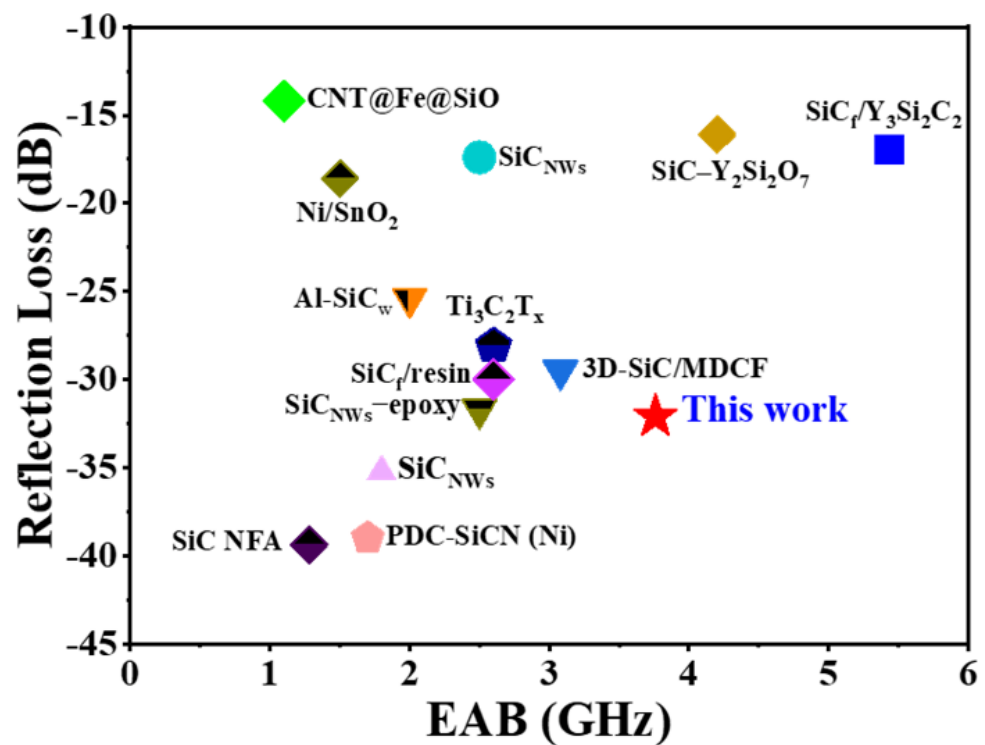


Figure 11. The comparison of EMW absorption properties of SiC<sub>w</sub>/Dy<sub>3</sub>Si<sub>2</sub>C<sub>2</sub> with other materials [3,23,29,66–75].

It can be concluded that the as-obtained  $\text{SiC}_w/\text{Dy}_3\text{Si}_2\text{C}_2$  whiskers could be a promising candidate for EMW absorbers for aerospace applications due to their excellent EMW absorption performance and wide EAB for thin samples, light weight, and potential oxidation resistance at high temperatures.

#### 4. Conclusions

In summary, a novel nano-laminated  $\text{Dy}_3\text{Si}_2\text{C}_2$  coating was in situ fabricated on the surface of  $\text{SiC}_w$  using the molten salt method to improve EMW absorption performance. A randomly stacked 2D  $\text{Dy}_3\text{Si}_2\text{C}_2$  nanosheet coating with a thickness of  $\sim 100$  nm was uniformly coated on the surface of 1D  $\text{SiC}_w$ , which further formed a 3D microstructure. The EMW absorption performance of the as-obtained 3D structural  $\text{SiC}_w/\text{Dy}_3\text{Si}_2\text{C}_2$  sample was significantly improved when compared to the pure  $\text{SiC}_w$  sample. The minimum RL value increased from  $-10.64$  dB for the pure  $\text{SiC}_w$  to  $-32.09$  dB for the  $\text{SiC}_w/\text{Dy}_3\text{Si}_2\text{C}_2$ . At the same time, the corresponding thickness of  $1.54$  mm was much thinner than that of the pure  $\text{SiC}_w$  ( $4.5$  mm). The possible EMW absorption mechanism of the as-obtained  $\text{SiC}_w/\text{Dy}_3\text{Si}_2\text{C}_2$  sample was ascribed to the synergic effect of favorable impedance matching, enhanced conductance loss, interfacial polarization, dipole polarization, and multiple scattering. The as-obtained 3D structural  $\text{SiC}_w/\text{Dy}_3\text{Si}_2\text{C}_2$  could be a candidate for EMW absorber applications due to its excellent EMW absorption performance and wide EAB for relatively thin samples, light weight, as well as potential oxidation and corrosion resistance at high temperatures.

**Author Contributions:** Conceptualization, X.Z.; Methodology, G.Q. and F.H.; Formal analysis, G.Q., Y.L., W.Z. and F.H.; Investigation, G.Q.; Data curation, Y.L. and H.X.; Writing—original draft, G.Q.; Writing—review & editing, W.Z. and X.Z.; Supervision, X.Z.; Project administration, X.Z.; Funding acquisition, X.Z. All authors have read and agreed to the published version of the manuscript.

**Funding:** This study was supported by the National Natural Science Foundation of China (Grant No. 12275337, 11975296, 52102122) and the Natural Science Foundation of Ningbo city (2021J199). We would like to recognize the support from the Ningbo 3315 Innovative Teams Program, China (Grant No. 2019A-14-C). Thanks for the financial support of Advanced Energy Science and Technology Guangdong Laboratory (No. HND20TDTHGC00).

**Institutional Review Board Statement:** Not applicable.

**Informed Consent Statement:** Not applicable.

**Data Availability Statement:** All research data already shared in the manuscript.

**Conflicts of Interest:** The authors declare that they have no known competing financial interests or personal relationships that could have appeared to influence the work reported in this paper.

#### References

1. Wei, H.; Yu, Y.; Jiang, F.; Xue, J.; Zhao, F.; Wang, Q. Carbon@SiC( $\text{SiC}_{\text{nw}}$ )- $\text{Sc}_2\text{Si}_2\text{O}_7$  ceramics with multiple loss mediums for improving electromagnetic shielding performance. *J. Eur. Ceram. Soc.* **2022**, *42*, 2274–2281. [\[CrossRef\]](#)
2. Wang, L.; Su, S.; Wang, Y.  $\text{Fe}_3\text{O}_4$ -Graphite Composites as a Microwave Absorber with Bimodal Microwave Absorption. *ACS Appl. Nano Mater.* **2022**, *5*, 17565–17575. [\[CrossRef\]](#)
3. Zhou, W.; Zhang, Y.; Li, Y.; Gou, Y.; Zhou, X. In-situ synthesis of ternary layered  $\text{Y}_3\text{Si}_2\text{C}_2$  ceramic on silicon carbide fiber for enhanced electromagnetic wave absorption. *Ceram. Int.* **2022**, *48*, 1908–1915. [\[CrossRef\]](#)
4. Du, B.; Cai, M.; Wang, X.; Qian, J.; He, C.; Shui, A. Enhanced electromagnetic wave absorption property of binary  $\text{ZnO}/\text{NiCo}_2\text{O}_4$  composites. *J. Adv. Ceram.* **2021**, *10*, 832–842. [\[CrossRef\]](#)
5. Pongmuksuwan, P.; Salayong, K.; Lertwiriyaprapa, T.; Kitisatorn, W. Electromagnetic Absorption and Mechanical Properties of Natural Rubber Composites Based on Conductive Carbon Black and  $\text{Fe}_3\text{O}_4$ . *Materials* **2022**, *15*, 6532. [\[CrossRef\]](#) [\[PubMed\]](#)
6. Mouchon, E.; Colomban, P. Microwave absorbent—Preparation, mechanical properties and rf-microwave conductivity of sic (and/or mullite) fibre reinforced nasicon matrix composites. *J. Mater. Sci.* **1996**, *31*, 323–334. [\[CrossRef\]](#)
7. Zhao, W.; Shao, G.; Jiang, M.; Zhao, B.; Wang, H.; Chen, D.; Xu, H.; Li, X.; Zhang, R.; An, L. Ultralight polymer-derived ceramic aerogels with wide bandwidth and effective electromagnetic absorption properties. *J. Eur. Ceram. Soc.* **2017**, *37*, 3973–3980. [\[CrossRef\]](#)



8. Xu, X.; Wang, Y.; Yue, Y.; Wang, C.; Xu, Z.; Liu, D. Core-shell MXene/nitrogen-doped C heterostructure for wide-band electromagnetic wave absorption at thin thickness. *Ceram. Int.* **2022**, *48*, 30317–30324. [\[CrossRef\]](#)
9. Huang, W.; Wang, S.; Yang, X.; Zhang, X.; Zhang, Y.; Pei, K.; Che, R. Temperature induced transformation of Co@C nanoparticle in 3D hierarchical core-shell nanofiber network for enhanced electromagnetic wave adsorption. *Carbon* **2022**, *195*, 44–56. [\[CrossRef\]](#)
10. Shu, Y.; Zhao, T.; Li, X.; Yang, L.; Cao, S.; Ahmad, A.; Jiang, T.; Luo, H.; Jing, Z.; Ain, N.U. Flower-like Co@CoO nanohybrids assembled by crisp-rice-like quadrangle flakes as high-performance electromagnetic wave absorber. *Appl. Surf. Sci.* **2022**, *597*, 153754. [\[CrossRef\]](#)
11. Zhai, N.; Luo, J.; Xiao, M.; Zhang, Y.; Yan, W.; Xu, Y. In situ construction of Co@nitrogen-doped carbon/Ni nanocomposite for broadband electromagnetic wave absorption. *Carbon* **2023**, *203*, 416–425. [\[CrossRef\]](#)
12. Trukhanov, S.V.; Trukhanov, A.V.; Kostishyn, V.G.; Panina, L.V.; Trukhanov, A.V.; Turchenko, V.A.; Tishkevich, D.I.; Trukhanova, E.L.; Oleynik, V.V.; Yakovenko, O.S.; et al. Magnetic, dielectric and microwave properties of the  $\text{BaFe}_{12-x}\text{Ga}_x\text{O}_{19}$  ( $x \leq 1.2$ ) solid solutions at room temperature. *J. Magn. Magn. Mater.* **2017**, *442*, 300–310. [\[CrossRef\]](#)
13. Bao, Y.; Guo, R.; Liu, C.; Li, S.; Ma, J. Design of magnetic triple-shell hollow structural  $\text{Fe}_3\text{O}_4/\text{FeCo}/\text{C}$  composite microspheres with broad bandwidth and excellent electromagnetic wave absorption performance. *Ceram. Int.* **2020**, *46*, 23932–23940. [\[CrossRef\]](#)
14. Xiang, Z.; Song, Y.; Xiong, J.; Pan, Z.; Wang, X.; Liu, L.; Liu, R.; Yang, H.; Lu, W. Enhanced electromagnetic wave absorption of nanoporous  $\text{Fe}_3\text{O}_4$ @carbon composites derived from metal-organic frameworks. *Carbon* **2019**, *142*, 20–31. [\[CrossRef\]](#)
15. Zdrovets, M.V.; Kozlovskiy, A.L.; Shlimas, D.I.; Borgekov, D.B. Phase transformations in  $\text{FeCo}-\text{Fe}_2\text{CoO}_4/\text{Co}_3\text{O}_4$ -spinel nanostructures as a result of thermal annealing and their practical application. *J. Mater. Sci. Mater. Electron.* **2021**, *32*, 16694–16705. [\[CrossRef\]](#)
16. Qian, Y.; Tao, Y.; Li, W.; Li, Y.; Xu, T.; Hao, J.; Jiang, Q.; Luo, Y.; Yang, J. High electromagnetic wave absorption and thermal management performance in 3D CNF@C-Ni/epoxy resin composites. *Chem. Eng. J.* **2021**, *425*, 131608. [\[CrossRef\]](#)
17. Xu, P.; He, H.; Fang, J.; Shang, T.; Wang, S.; Ge, S.; Wu, S.; Yue, X. Design and fabrication of a hollow nanobowl-like heterostructured PPy@Co/CoFe<sub>2</sub>O<sub>4</sub>@HNBC composite as a remarkable electromagnetic wave absorber. *J. Alloys Compd.* **2022**, *926*, 166749. [\[CrossRef\]](#)
18. Xia, C.; Zhang, S.; Ren, H.; Shi, S.Q.; Zhang, H.; Cai, L.; Li, J. Scalable fabrication of natural-fiber reinforced composites with electromagnetic interference shielding properties by incorporating powdered activated carbon. *Materials* **2015**, *9*, 10. [\[CrossRef\]](#)
19. Jacobson, N.S.; Curry, D.M. Oxidation microstructure studies of reinforced carbon/carbon. *Carbon* **2006**, *44*, 1142–1150. [\[CrossRef\]](#)
20. Wen, B.; Cao, M.; Lu, M.; Cao, W.; Shi, H.; Liu, J.; Wang, X.; Jin, H.; Fang, X.; Wang, W. Reduced graphene oxides: Light-weight and high-efficiency electromagnetic interference shielding at elevated temperatures. *Adv. Mater.* **2014**, *26*, 3484–3489. [\[CrossRef\]](#)
21. Zhou, X.; Jing, L.; Kwon, Y.D.; Kim, J.-Y.; Huang, Z.; Yoon, D.-H.; Lee, J.; Huang, Q. Fabrication of  $\text{SiC}_w/\text{Ti}_3\text{SiC}_2$  composites with improved thermal conductivity and mechanical properties using spark plasma sintering. *J. Adv. Ceram.* **2020**, *9*, 462–470. [\[CrossRef\]](#)
22. He, R.; Zhou, N.; Zhang, K.; Zhang, X.; Zhang, L.; Wang, W.; Fang, D. Progress and challenges towards additive manufacturing of SiC ceramic. *J. Adv. Ceram.* **2021**, *10*, 637–674. [\[CrossRef\]](#)
23. Wang, C.; Chen, L.; He, H.; Ye, T.; Deng, Q.; Wei, H.; Zhao, F.; Wang, Q. Nano-SiC-decorated  $\text{Y}_2\text{Si}_2\text{O}_7$  ceramic for enhancing electromagnetic waves absorption performance. *Ceram. Int.* **2022**, *48*, 20168–20175. [\[CrossRef\]](#)
24. Song, C.; Liu, Y.; Ye, F.; Cheng, L.; Zhang, P.; Chai, N. Enhanced mechanical property and tunable dielectric property of SiC f/SiC-SiBCN composites by CVI combined with PIP. *J. Adv. Ceram.* **2021**, *10*, 758–767. [\[CrossRef\]](#)
25. Zhou, Q.; Yin, X.; Ye, F.; Tang, Z.; Mo, R.; Cheng, L. High temperature electromagnetic wave absorption properties of  $\text{SiC}_f/\text{Si}_3\text{N}_4$  composite induced by different SiC fibers. *Ceram. Int.* **2019**, *45*, 6514–6522. [\[CrossRef\]](#)
26. Yuan, K.; Han, D.; Liang, J.; Zhao, W.; Li, M.; Zhao, B.; Liu, W.; Lu, H.; Wang, H.; Xu, H. Microwave induced in-situ formation of SiC nanowires on SiCNO ceramic aerogels with excellent electromagnetic wave absorption performance. *J. Adv. Ceram.* **2021**, *10*, 1140–1151. [\[CrossRef\]](#)
27. Dong, S.; Zhang, W.; Zhang, X.; Hu, P.; Han, J. Designable synthesis of core-shell  $\text{SiC}_w$ @C heterostructures with thickness-dependent electromagnetic wave absorption between the whole X-band and Ku-band. *Chem. Eng. J.* **2018**, *354*, 767–776. [\[CrossRef\]](#)
28. Cai, Z.; Su, L.; Wang, H.; Xie, Q.; Gao, H.; Niu, M.; Lu, D. Hierarchically assembled carbon microtube@SiC nanowire/Ni nanoparticle aerogel for highly efficient electromagnetic wave absorption and multifunction. *Carbon* **2022**, *191*, 227–235. [\[CrossRef\]](#)
29. Kuang, J.; Jiang, P.; Ran, F.; Cao, W. Conductivity-dependent dielectric properties and microwave absorption of Al-doped SiC whiskers. *J. Alloys Compd.* **2016**, *687*, 227–231. [\[CrossRef\]](#)
30. Lv, X.; Ye, F.; Cheng, L.; Zhang, L. 3D printing “wire-on-sphere” hierarchical SiC nanowires/SiC whiskers foam for efficient high-temperature electromagnetic wave absorption. *J. Mater. Sci. Technol.* **2022**, *109*, 94–104. [\[CrossRef\]](#)
31. Wen, J.; Li, X.; Zhang, H.; Chen, M.; Wu, X. Enhancement of solar absorption performance using  $\text{TiN}/\text{SiC}_w$  plasmonic nanofluids for effective photo-thermal conversion: Numerical and experimental investigation. *Renew. Energy* **2022**, *193*, 1062–1073. [\[CrossRef\]](#)
32. Wang, P.; Cheng, L.; Zhang, Y.; Zhang, L. Flexible  $\text{SiC}/\text{Si}_3\text{N}_4$  composite nanofibers with in situ embedded graphite for highly efficient electromagnetic wave absorption. *ACS Appl. Mater. Interfaces* **2017**, *9*, 28844–28858. [\[CrossRef\]](#) [\[PubMed\]](#)
33. Bi, J.; Gu, Y.; Zhang, Z.; Wang, S.; Li, M.; Zhang, Z. Core-shell SiC/SiO<sub>2</sub> whisker reinforced polymer composite with high dielectric permittivity and low dielectric loss. *Mater. Des.* **2016**, *89*, 933–940. [\[CrossRef\]](#)

34. Dong, S.; Zhang, X.; Hu, P.; Zhang, W.; Han, J.; Hu, P. Biomass-derived carbon and polypyrrole addition on SiC whiskers for enhancement of electromagnetic wave absorption. *Chem. Eng. J.* **2019**, *359*, 882–893. [\[CrossRef\]](#)
35. Chen, J.-P.; Du, Y.-F.; Wang, Z.-F.; Liang, L.-L.; Jia, H.; Liu, Z.; Xie, L.-J.; Zhang, S.-C.; Chen, C.-M. Anchoring of SiC whiskers on the hollow carbon microspheres inducing interfacial polarization to promote electromagnetic wave attenuation capability. *Carbon* **2021**, *175*, 11–19. [\[CrossRef\]](#)
36. Dong, S.; Lyu, Y.; Li, X.; Chen, J.; Zhang, X.; Han, J.; Hu, P. Construction of MnO nanoparticles anchored on SiC whiskers for superior electromagnetic wave absorption. *J. Colloid Interface Sci.* **2020**, *559*, 186–196. [\[CrossRef\]](#)
37. Gerdes, M.H.; Witte, A.M.; Jeitschko, W.; Lang, A.; Künne, B. Magnetic and Electrical Properties of a New Series of Rare Earth Silicide Carbides with the Composition  $R_3Si_2C_2$  ( $R = Y, La-Nd, Sm, Gd-Tm$ ). *J. Solid State Chem.* **1998**, *138*, 201–206. [\[CrossRef\]](#)
38. Jeitschko, W.; Gerdes, M.H.; Witte, A.M.; Rodewald, U.C. Subcell structure and two different superstructures of the rare earth metal silicide carbides  $Y_3Si_2C_2$ ,  $Pr_3Si_2C_2$ ,  $Tb_3Si_2C_2$ , and  $Dy_3Si_2C_2$ . *J. Solid State Chem.* **2001**, *156*, 1–9. [\[CrossRef\]](#)
39. Xu, K.; Chang, K.; Zhou, X.; Chen, L.; Liu, J.; Deng, Z.; Huang, F.; Huang, Q. Thermodynamic descriptions of the light rare-earth elements in silicon carbide ceramics. *J. Am. Ceram. Soc.* **2020**, *103*, 3812–3825. [\[CrossRef\]](#)
40. Liu, J.; Zhou, X.; Tatarko, P.; Yuan, Q.; Zhang, L.; Wang, H.; Huang, Z.; Huang, Q. Fabrication, microstructure, and properties of SiC/ $Al_4SiC_4$  multiphase ceramics via an in-situ formed liquid phase sintering. *J. Adv. Ceram.* **2020**, *9*, 193–203. [\[CrossRef\]](#)
41. Shi, L.-K.; Zhou, X.; Dai, J.-Q.; Chen, K.; Huang, Z.; Huang, Q. Microstructure and properties of nano-laminated  $Y_3Si_2C_2$  ceramics fabricated via in situ reaction by spark plasma sintering. *J. Adv. Ceram.* **2021**, *10*, 578–586. [\[CrossRef\]](#)
42. Zhou, X.; Liu, J.; Zou, S.; Xu, K.; Chang, K.; Li, P.; Huang, F.; Huang, Z.; Huang, Q. Almost seamless joining of SiC using an in-situ reaction transition phase of  $Y_3Si_2C_2$ . *J. Eur. Ceram. Soc.* **2020**, *40*, 259–266. [\[CrossRef\]](#)
43. Yu, T.; Xu, J.; Zhou, X.; Tatarko, P.; Li, Y.; Huang, Z.; Huang, Q. Near-seamless joining of Cf/SiC composites using  $Y_3Si_2C_2$  via electric field-assisted sintering technique. *J. Adv. Ceram.* **2022**, *11*, 1196–1207. [\[CrossRef\]](#)
44. Shi, L.-K.; Zhou, X.; Xu, K.; Chang, K.; Dai, J.-Q.; Huang, Z.; Huang, Q. Low temperature seamless joining of SiC using a Ytterbium film. *J. Eur. Ceram. Soc.* **2021**, *41*, 7507–7515. [\[CrossRef\]](#)
45. Xu, J.; Zhou, X.; Zou, S.; Chen, L.; Tatarko, P.; Dai, J.Q.; Huang, Z.; Huang, Q. Low-temperature  $Pr_3Si_2C_2$ -assisted liquid-phase sintering of SiC with improved thermal conductivity. *J. Am. Ceram. Soc.* **2022**, *105*, 5576–5584. [\[CrossRef\]](#)
46. Zhou, X.; Yu, T.; Xu, J.; Li, Y.; Huang, Z.; Huang, Q. Ultrafast low-temperature near-seamless joining of Cf/SiC using a sacrificial  $Pr_3Si_2C_2$  filler via electric current field-assisted sintering technique. *J. Eur. Ceram. Soc.* **2022**, *42*, 6865–6875. [\[CrossRef\]](#)
47. Yakovenko, O.S.; Matzui, L.Y.; Vovchenko, L.L.; Trukhanov, A.V.; Kazakevich, I.S.; Trukhanov, S.V.; Prylutsky, Y.I.; Ritter, U. Magnetic anisotropy of the graphite nanoplatelet-epoxy and MWCNT-epoxy composites with aligned barium ferrite filler. *J. Mat. Sci.* **2017**, *52*, 5345–5358. [\[CrossRef\]](#)
48. Kozlovskiy, A.L.; Shlimas, D.I.; Zdorovets, M.V. Synthesis, structural properties and shielding efficiency of glasses based on  $TeO_2-(1-x)ZnO-xSm_2O_3$ . *J. Mater. Sci. Mater. Electron.* **2021**, *32*, 12111–12120. [\[CrossRef\]](#)
49. Liu, P.; Ma, T.; Wang, X.; Zhang, Y.; Yan, M. Role of hydrogen in Nd-Fe-B sintered magnets with DyHx addition. *J. Alloys Compd.* **2015**, *628*, 282–286. [\[CrossRef\]](#)
50. Liu, X.; Fechner, N.; Antonietti, M. Salt melt synthesis of ceramics, semiconductors and carbon nanostructures. *Chem. Soc. Rev.* **2013**, *42*, 8237–8265. [\[CrossRef\]](#)
51. Liu, D.; Fu, Q.; Chu, Y. Molten salt synthesis, formation mechanism, and oxidation behavior of nanocrystalline  $HfB_2$  powders. *J. Adv. Ceram.* **2020**, *9*, 35–44. [\[CrossRef\]](#)
52. Debye, P. *Polar Molecules*; The Chemical Catalog Company, Inc.: New York, NY, USA, 1929; pp. 77–108.
53. Moitra, D.; Chandel, M.; Ghosh, B.K.; Jani, R.K.; Patra, M.K.; Vadera, S.R.; Ghosh, N.N. A simple ‘in situ’ co-precipitation method for the preparation of multifunctional  $CoFe_2O_4$ -reduced graphene oxide nanocomposites: Excellent microwave absorber and highly efficient magnetically separable recyclable photocatalyst for dye degradation. *RSC Adv.* **2016**, *6*, 76759–76772. [\[CrossRef\]](#)
54. Kingery, W.D.; Bowen, H.K.; Uhlmann, D.R. *Introduction to Ceramics*; John Wiley & Sons: Hoboken, NJ, USA, 1976; Volume 17.
55. Wang, Y.; Zhou, W.; Zeng, G.; Chen, H.; Luo, H.; Fan, X.; Li, Y. Rational design of multi-shell hollow carbon microspheres for high-performance microwave absorbers. *Carbon* **2021**, *175*, 233–242. [\[CrossRef\]](#)
56. Lou, Z.; Yuan, C.; Zhang, Y.; Li, Y.; Cai, J.; Yang, L.; Wang, W.; Han, H.; Zou, J. Synthesis of porous carbon matrix with inlaid  $Fe_3C/Fe_3O_4$  micro-particles as an effective electromagnetic wave absorber from natural wood shavings. *J. Alloys Compd.* **2019**, *775*, 800–809. [\[CrossRef\]](#)
57. Wen, B.; Cao, M.-S.; Hou, Z.-L.; Song, W.-L.; Zhang, L.; Lu, M.-M.; Jin, H.-B.; Fang, X.-Y.; Wang, W.-Z.; Yuan, J. Temperature dependent microwave attenuation behavior for carbon-nanotube/silica composites. *Carbon* **2013**, *65*, 124–139. [\[CrossRef\]](#)
58. Duan, Y.; Guan, H. *Microwave Absorbing Materials*; CRC Press: Boca Raton, FL, USA, 2016. [\[CrossRef\]](#)
59. Kim, S.; Jo, S.; Gueon, K.; Choi, K.; Kim, J.; Churn, K. Complex permeability and permittivity and microwave absorption of ferrite-rubber composite at X-band frequencies. *IEEE Trans. Magn.* **1991**, *27*, 5462–5464. [\[CrossRef\]](#)
60. Zhang, W.; Zhang, X.; Zheng, Y.; Guo, C.; Yang, M.; Li, Z.; Wu, H.; Qiu, H.; Yan, H.; Qi, S. Preparation of polyaniline@ $MoS_2$ @ $Fe_3O_4$  nanowires with a wide band and small thickness toward enhancement in microwave absorption. *ACS Appl. Nano Mater.* **2018**, *1*, 5865–5875. [\[CrossRef\]](#)
61. Yuan, X.; Li, H.; Sha, A.; Huang, S.; Li, B.; Guo, S. Flexible  $Mo_2C$ -Modified SiC/C Nanofibers for BroadBand Electromagnetic Wave Absorption. *Adv. Mater. Interfaces* **2022**, *9*, 2200333. [\[CrossRef\]](#)

62. Fan, B.; Ansar, M.T.; Wang, X.; Song, L.; Du, H.; Lu, H.; Zhao, B.; Zhang, R.; Fan, L.; Li, H. Two-Dimensional C/MoS<sub>2</sub>-Functionalized Ti<sub>3</sub>C<sub>2</sub>T<sub>x</sub> Nanosheets for Achieving Strong Electromagnetic Wave Absorption. *Adv. Electron. Mater.* **2022**, *8*, 2200169. [\[CrossRef\]](#)
63. He, P.; Cao, M.-S.; Cao, W.-Q.; Yuan, J. Developing MXenes from wireless communication to electromagnetic attenuation. *Nano-Micro Lett.* **2021**, *13*, 115. [\[CrossRef\]](#)
64. Li, Y.; Meng, F.; Mei, Y.; Wang, H.; Guo, Y.; Wang, Y.; Peng, F.; Huang, F.; Zhou, Z. Electrospun generation of Ti<sub>3</sub>C<sub>2</sub>T<sub>x</sub> MXene@graphene oxide hybrid aerogel microspheres for tunable high-performance microwave absorption. *Chem. Eng. J.* **2020**, *391*, 123512. [\[CrossRef\]](#)
65. Hu, Q.; Yang, R.; Mo, Z.; Lu, D.; Yang, L.; He, Z.; Zhu, H.; Tang, Z.; Gui, X. Nitrogen-doped and Fe-filled CNTs/NiCo<sub>2</sub>O<sub>4</sub> porous sponge with tunable microwave absorption performance. *Carbon* **2019**, *153*, 737–744. [\[CrossRef\]](#)
66. Wu, R.; Zhou, K.; Yang, Z.; Qian, X.; Wei, J.; Liu, L.; Huang, Y.; Kong, L.; Wang, L. Molten-salt-mediated synthesis of SiC nanowires for microwave absorption applications. *CrystEngComm* **2013**, *15*, 570–576. [\[CrossRef\]](#)
67. Chiu, S.-C.; Yu, H.-C.; Li, Y.-Y. High electromagnetic wave absorption performance of silicon carbide nanowires in the gigahertz range. *J. Phys. Chem. C* **2010**, *114*, 1947–1952. [\[CrossRef\]](#)
68. Ye, X.; Chen, Z.; Ai, S.; Hou, B.; Zhang, J.; Liang, X.; Zhou, Q.; Liu, H.; Cui, S. Porous SiC/melamine-derived carbon foam frameworks with excellent electromagnetic wave absorbing capacity. *J. Adv. Ceram.* **2019**, *8*, 479–488. [\[CrossRef\]](#)
69. Kuang, J.; Xiao, T.; Hou, X.; Zheng, Q.; Wang, Q.; Jiang, P.; Cao, W. Microwave synthesis of worm-like SiC nanowires for thin electromagnetic wave absorbing materials. *Ceram. Int.* **2019**, *45*, 11660–11667. [\[CrossRef\]](#)
70. Xu, W.; Li, S.; Hu, S.; Yu, W.; Zhou, Y. Effect of Ti<sub>3</sub>AlC<sub>2</sub> precursor and processing conditions on microwave absorption performance of resultant Ti<sub>3</sub>C<sub>2</sub>T<sub>x</sub> MXene. *J. Mater. Sci.* **2021**, *56*, 9287–9301. [\[CrossRef\]](#)
71. Liu, Y.; Feng, Y.; Gong, H.; Zhang, Y.; Lin, X.; Xie, B.; Mao, J. Electromagnetic wave absorption properties of nickel-containing polymer-derived SiCN ceramics. *Ceram. Int.* **2018**, *44*, 10945–10950. [\[CrossRef\]](#)
72. Song, L.; Fan, B.; Chen, Y.; Wang, H.; Li, H.; Zhang, R. Multifunctional SiC nanofiber aerogel with superior electromagnetic wave absorption. *Ceram. Int.* **2022**, *48*, 25140–25150. [\[CrossRef\]](#)
73. Liu, X.; Zhang, L.; Yin, X.; Ye, F.; Liu, Y.; Cheng, L. The microstructure and electromagnetic wave absorption properties of near-stoichiometric SiC fibre. *Ceram. Int.* **2017**, *43*, 3267–3273. [\[CrossRef\]](#)
74. Lv, H.; Ji, G.; Zhang, H.; Du, Y. Facile synthesis of a CNT@Fe@SiO<sub>2</sub> ternary composite with enhanced microwave absorption performance. *RSC Adv.* **2015**, *5*, 76836–76843. [\[CrossRef\]](#)
75. Zhao, B.; Shao, G.; Fan, B.; Li, W.; Pian, X.; Zhang, R. Enhanced electromagnetic wave absorption properties of Ni-SnO<sub>2</sub> core-shell composites synthesized by a simple hydrothermal method. *Mater. Lett.* **2014**, *121*, 118–121. [\[CrossRef\]](#)

**Disclaimer/Publisher's Note:** The statements, opinions and data contained in all publications are solely those of the individual author(s) and contributor(s) and not of MDPI and/or the editor(s). MDPI and/or the editor(s) disclaim responsibility for any injury to people or property resulting from any ideas, methods, instructions or products referred to in the content.